To support the suggestion that local chemical changes are induced at the inclusion, we find significant compositional variations within the inclusions themselves as can be seen in the mass spectra (Fig. 3a). Several inclusions show an outer ring that is rich in Mn and Cr. In addition, we find that many inclusions show clear crystallographic features, localized high concentration of Cr and evidence of voids within the inclusion (Fig. 3c, d).

We intend to quantify the depletion effects and develop methods of assessing such local changes in and around second-phase precipitates in this and other heterogeneous alloy systems.

The data we have shown provides direct evidence for the mechanism that operates in the pitting corrosion of stainless steels that is consistent with the large body of corrosion literature[22]. A localized zone exists that is known to display enhanced electrochemical activity and we relate this directly to local chemical variations. This critical zone is a region that is on the order of only 200–400 nm across, yet is responsible for some of the most catastrophic failures of metallic structures. Our findings also focus on the steel processing conditions that allow the set-up of local depleted zones, and hence suggest methods of minimizing the likelihood of pitting corrosion. □

Received 5 November; accepted 19 December 2001.

1. Williams, D. E., Westcott, C. & Fleischmann, M. Stochastic models of pitting corrosion of stainless steels. 1. Modeling of the initiation and growth of pits at constant potential. *J. Electrochem. Soc.* **132,** 1796–1804 (1985).
2. Eklund, G. S. Initiation of pitting at sulfide inclusions in stainless steel. *J. Electrochem. Soc.* **121,** 467–473 (1974).
3. Wranglen, G. Pitting and sulphide inclusions in steel. *Corrosion Sci.* **14,** 331–349 (1974).
4. Williams, D. E. & Zhu, Y. Y. Explanation for initiation of pitting corrosion of stainless steels at sulfide inclusions. *J. Electrochem. Soc.* **147,** 1763–1766 (2000).
5. Galvele, J. R. Transport processes and the mechanism of pitting of metals. *J. Electrochem. Soc.* **123,** 464–474 (1976).
6. Hoar, T. P., Mears, D. C. & Rothwell, G. P. The relationships between anodic passivity, brightening and pitting. *Corrosion Sci.* **5,** 279–289 (1981).
7. Chao, C. Y., Lin, L. F. & Macdonald, D. D. A point defect model for anodic passive films. *J. Electrochem. Soc.* **128,** 1187–1194 (1981).
8. Uhlig, H. H. Adsorbed and reaction-production films on metals. *J. Electrochem. Soc.* **97,** 215C (1950).
9. Sato, N. A. Theory for breakdown of anodic oxide films on metals. *Electrochim. Acta.* **16,** 1683–1692 (1971).
10. Richardson, J. A. & Wood, G. C. Study of the pitting corrosion of Al by scanning electron microscopy. *Corrosion Sci.* **10,** 313–323 (1970).
11. Suter, T. & Bohni, H. Microelectrodes for corrosion studies in microsystems. *Electrochim. Acta* **47,** 191–199 (2001).
12. Lott, S. E. & Alkire, R. C. The role of inclusions on initiation of crevice corrosion of stainless steel. 1. Experimental studies. *J. Electrochem. Soc.* **136,** 973–979 (1989).
13. Marcus, P., Teissier, A. & Oudar, J. The influence of sulphur on the dissolution and passivation of a NiFe Alloy. 1. Electrochemical and radio tracer measurements. *Corrosion Sci.* **24,** 259–268 (1984).
14. Baker, M. A. & Castle, J. E. The initiation of pitting corrosion at MnS inclusions. *Corrosion Sci.* **34,** 667–682 (1993).
15. Ryan, M. P., Laycock, N. J., Newman, R. C. & Isaacs, H. S. The pitting behaviour of thin film FeCr alloys in hydrochloric acid. *J. Electrochem. Soc.* **145,** 1566–1571 (1998).
16. Stewart, J. & Williams, D. E. The initiation of pitting corrosion on austenitic stainless steels: on the role and importance of sulphide inclusions. *Corrosion Sci.* **33,** 457–474 (1992).
17. Monnartz, P. Iron–chromium alloys with special consideration of resistance to acids. *Metallurgie* **8,** 161–176 (1911).
18. Williams, D. E., Newman, R. C., Song, Q. & Kelly, R. G. Passivity breakdown and pitting corrosion of binary alloys. *Nature* **350,** 216–219 (1991).
19. Webb, E. G., Suter, T. & Alkire, R. C. Microelectrochemical measurements of the dissolution of single MnS inclusions, and the prediction of critical conditions for pit initiation on stainless steel. *J. Electrochem. Soc.* **148,** B186–B195 (2001).
20. Williams, D. E., Mohiuddin, T. F. & Zhu, Y. Elucidation of a trigger mechanism for pitting corrosion of stainless steels using sub-micron resolution SECM and photoelectrochemical microscopy. *J. Electrochem. Soc.* **145,** 2664–2672 (1998).
21. Brossia, C. S. & Kelly, R. G. Influence of sulfur content and bulk electrolyte composition on crevice corrosion initiation of austenitic stainless steel. *Corrosion* **54,** 145–154 (1998).
22. Frankel, G. S. Pitting corrosion of metals: a review of the critical factors. *J. Electrochem. Soc.* **145,** 2186–2197 (1998).

Acknowledgements

This work was supported by the Engineering and Physical Sciences Research Council, UK.

Competing interests statement

The authors declare that they have no competing financial interests.

Correspondence and requests for materials should be addressed to M.P.R. (e-mail: m.p.ryan@ic.ac.uk).

Poleward heat transport by the atmospheric heat engine

Leon Barry, George C. Craig & John Thuburn

Department of Meteorology, University of Reading, Earley Gate, Whiteknights, Reading RG6 6BB, UK

The atmospheric heat transport on Earth from the Equator to the poles is largely carried out by the mid-latitude storms. However, there is no satisfactory theory to describe this fundamental feature of the Earth's climate[1,2]. Previous studies have characterized the poleward heat transport as a diffusion by eddies of specified horizontal length and velocity scales, but there is little agreement as to what those scales should be[3–7]. Here we propose instead to regard the baroclinic zone—the zone of strong temperature gradients and active eddies—as a heat engine which generates eddy kinetic energy by transporting heat from a warmer to a colder region. This view leads to a new velocity scale, which we have tested along with previously proposed length and velocity scales, using numerical climate simulations in which the eddy properties have been varied by changing forcing and boundary conditions. The experiments show that the eddy velocity varies in accordance with the new scale, while the size of the eddies varies with the well-known Rhines β-scale. Our results not only give new insight into atmospheric eddy heat transport, but also allow simple estimates of the intensities of mid-latitude storms, which have hitherto only been possible with expensive general circulation models.

The poleward eddy heat transport in a planetary atmosphere can be written as the vertical integral of $\overline{v'T'} = k|v'||T'|$, where overbar means a zonal average, prime means a departure from the zonal average, $||$ means a root-mean-square magnitude, and k is the correlation between the meridional eddy velocity v' and the eddy temperature perturbation T'. If it is assumed that $|T'| = -L_{\mathrm{disp}}\overline{T}_y$, where $\overline{T}_y$ is the poleward temperature gradient and L_{disp} is a typical meridional fluid parcel displacement, then $\overline{v'T'} = -D\overline{T}_y$ where the transport coefficient $D = L_{\mathrm{disp}}|v'|$. These flux-gradient theories generally assume that the correlation k is constant[3–5], and attempt to predict characteristic scales L_{disp} and $|v'|$ that will occur on a given zonal-mean state. We found the constant-k assumption to hold to a good approximation for the experiments discussed below; k was in the range 0.2–0.35 despite variations in the heat flux of about two orders of magnitude[8]. A constant value $k = 0.25$ is used in all subsequent calculations. It is currently an open question whether a flux-gradient relation can give useful quantitative predictions of eddy heat transport, because it requires the assumption that L_{disp} is much smaller than the width of the baroclinic zone[9]. The results below imply that this is true for the Earth.

Table 1 Summary of diffusivity parameters

Theory	L	$\|v'\|$	D
Stone[4]	L_{D}	$\overline{u}$	$k\overline{u}L_{\mathrm{D}}$
Green[3]	L_{zone}	$\overline{u}L_{\mathrm{zone}}/L_{\mathrm{D}}$	$k\overline{u}L_{\mathrm{zone}}^2/L_{\mathrm{D}}$
Haine and Marshall[7]	L_{zone}	$\overline{u}$	$k\overline{u}L_{\mathrm{zone}}$
Held and Larichev[6]	L_β	$\overline{u}\gamma^{-1}$	$k\overline{u}L_{\mathrm{D}}\gamma^{-2}$
Branscome[5,13]	$\frac{L_{\mathrm{D}}}{(0.48+1.48\gamma)}$	$\frac{\overline{u}}{(0.48+1.48\gamma)}$	$\frac{k\overline{u}L_{\mathrm{D}}}{(0.48+1.48\gamma)}$
This work	L_β	$\left(\frac{ea\overline{T}_y q}{T_0}\right)^{2/5}\left(\frac{2}{\beta}\right)^{1/5}$	$\left(\frac{ea\overline{T}_y q}{T_0}\right)^{3/5}\left(\frac{2}{\beta}\right)^{4/5}$

$L_{\mathrm{D}} = NH/f$, $L_\beta = (2|v'|/\beta)^{1/2}$ and $\gamma = \beta\theta_z H/(f\theta_y)$.

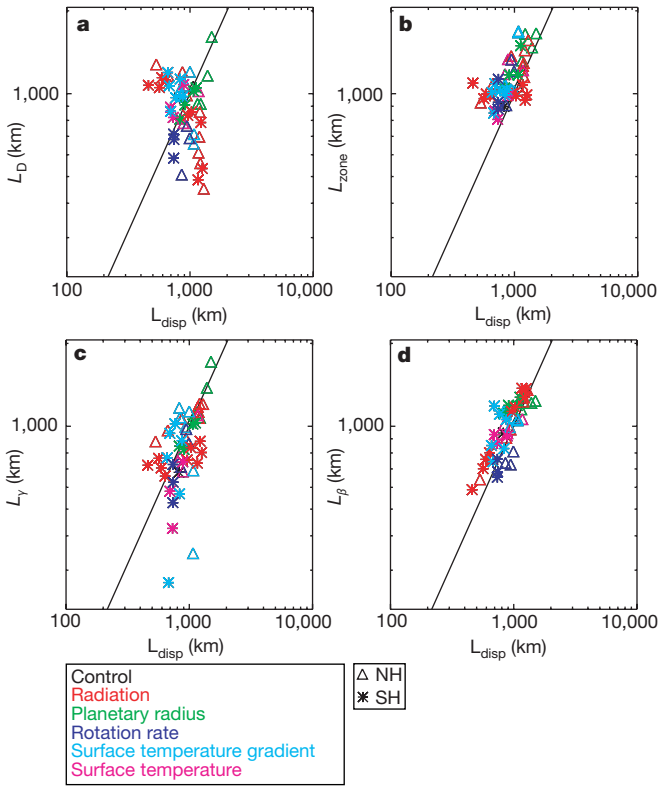

Figure 1 Predicted length scales versus diagnosed eddy length scale $L_{disp} = \overline{v'T'}/(k\overline{T}_y|v'|)$. The four predicted length scales are: **a**, $L_D = NH/f$, the radius of deformation; **b**, L_{zone}, the size of the baroclinic zone; **c**, $L_\gamma = L_D/(0.48 + 1.48\gamma)$ where $\gamma = (\beta\theta_z H_s)/(f\theta_y)$; and **d**, $L_\beta = (2|v'|/\beta)^{1/2}$ is the Rhines β-scale. The four length scales have been normalized so that they are equal to L_{disp} for the Northern Hemisphere of the control climate. Symbol type represents the hemisphere, colour represents the type of experiment. NH, Northern Hemisphere; SH, Southern Hemisphere.

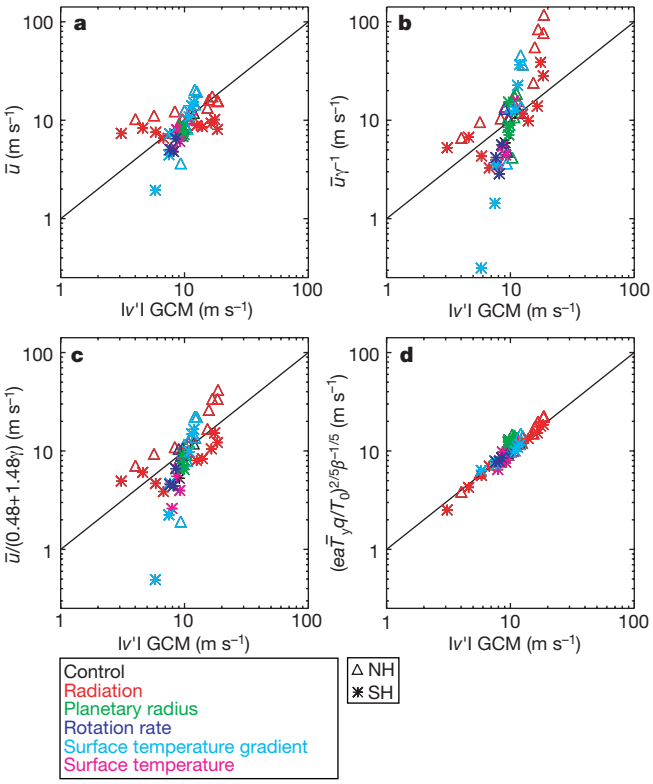

Figure 2 Predicted velocity scales versus diagnosed eddy velocity scale $|v'|$. The four predicted velocity scales are $\overline{u}$ (**a**), $\overline{u}\gamma^{-1}$ (**b**), $\overline{u}/(0.48 + 1.48\gamma)$ (**c**) and $(ea\overline{T}_y q/T_0)^{2/5}(2/\beta)^{1/5}$ (**d**) (Symbols are defined in the text.). The four velocity scales have been normalized so that they are equal to $|v'|$ for the Northern Hemisphere of the control climate. Symbol type and colour have same meaning as in Fig. 1. GCM, general circulation model.

Different assumptions about the dominant physical processes in the atmosphere lead to very different predictions for L_{disp} and $|v'|$. The turbulent eddies that transport heat extract energy from the mean flow primarily through baroclinic instability, suggesting that a plausible prediction for L_{disp} may be obtained from the size of the fastest-growing wave found in a linear model of this process. The fastest-growing wave in the Eady model[10], one of the simplest analytic models of baroclinic instability, has zonal length scale proportional to the radius of deformation $L_D = NH/f$, where N is the buoyancy frequency, H is the depth of the domain (in this case the troposphere) and f is the Coriolis parameter, defined as $2\Omega\sin\phi$, where Ω is the Earth's rotation rate, and ϕ is the latitude. If nonlinear interactions are assumed to make the eddies circular, then the meridional scale will be proportional to L_D too[4]. An alternative model of baroclinic instability is the Charney model[11], in which an approximation to the fastest-growing mode has a horizontal length scale[5,12,13] $L_\gamma = (NH_s/f)/(0.48 + 1.48\gamma)$, where $\gamma = \beta\theta_z H_s/f\theta_y$. In this expression, H_s is the density scale height, $\beta = f_y$ is the northward gradient of f, and θ_z and θ_y are the vertical and horizontal derivatives of the potential temperature $\theta = T(p_o/p)^\kappa$, where p_o is a reference pressure of 1,000 mbar and $\kappa = R/c_p$ is the ratio of the gas constant for dry air to the specific heat at constant pressure. However, the main energy-containing eddy scale will not necessarily be that of the fastest-growing baroclinic mode. Other candidate length scales are suggested by geostrophic turbulence theory, which postulates a cascade of energy to larger horizontal scales[14,15] that may dominate the heat transport. The largest scale to which a cascade could extend is L_{zone}, the size of the baroclinic zone[3,16]. A final possibility is that the cascade to larger scales may be halted before L_{zone} at the Rhines β-scale $L_\beta = (2|v'|/\beta)^{1/2}$, the scale at which the Rossby wave restoring mechanism becomes comparable to advective nonlinearity[17].

A plausible estimate for the eddy velocity scale is that it is proportional to the speed of the zonal mean flow[7,18], that is, $|v'| \propto \overline{u}$. However, it has also been suggested that there should be an equipartition between eddy potential energy and eddy kinetic energy[4,6], which can be shown to lead to the relation $|v'| \propto \overline{u}(L_{disp}/L_D)$. These scales depend upon the local properties of the zonal mean state.

We propose an alternative velocity scale that comes from a thermodynamic constraint on the baroclinic zone as a whole. This is obtained by considering the baroclinic zone (rather than the global atmosphere, as previously proposed[19]) as a heat engine that obtains its kinetic energy in the process of transporting heat from a warmer to a colder region. The rate of generation and dissipation of eddy kinetic energy is given by $\epsilon = e(\delta T/T_0)q$, where q is the rate of energy transport out of the tropics, calculated as the net diabatic (radiative plus surface flux) cooling per unit mass averaged over the baroclinic zone, $\delta T/T_0$ is the maximum possible thermodynamic efficiency, δT is the temperature difference between the regions where the heat is put in and where it is extracted, and e is the utilization coefficient (assumed constant), which measures the fraction of the generated kinetic energy used by heat-transporting eddies. If the heat-transporting eddies exist in an inertial range, for example in the postulated upscale energy cascade, then the average properties of the flow will depend only on the dissipation rate

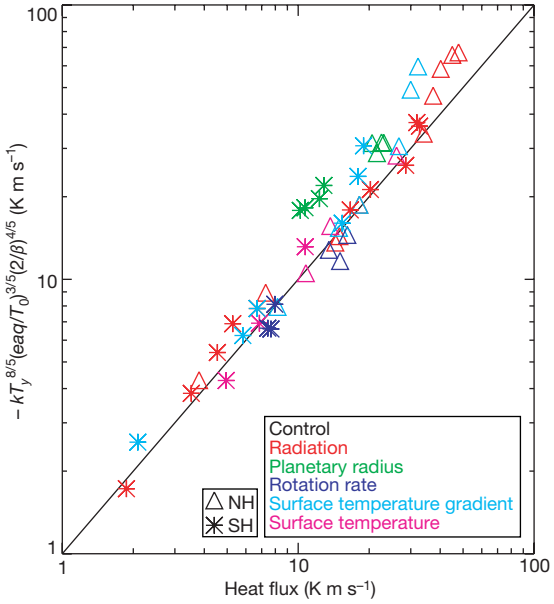

Figure 3 Parametrized heat flux versus heat flux diagnosed directly from the GCM. The heat flux predicted by the new parametrization is $\overline{v'T'}_{\text{param}} = k\overline{T}_y^{8/5}(eaq/T_0)^{3/5}(2/\beta)^{4/5}$. The predicted flux has been normalized so that it is equal to the GCM flux for the Northern Hemisphere of the control climate. The symbol type and colour have the same meanings as in Fig. 1.

and the wavelength. This implies a scaling for the velocity of $|v'| \propto (\epsilon L_{\text{disp}})^{1/3}$. If we compare the two expressions involving ϵ and assume that $\delta T \propto a|\overline{T}_y|$ where a is the radius of the Earth, and anticipate the result that $L_{\text{disp}} \propto L_\beta$, then this leads to the expression $|v'| \propto (ea|\overline{T}_y|q/T_0)^{2/5}(2/\beta)^{1/5}$.

The various velocity and length scales introduced above have been used to define a number of heat flux parametrizations, as summarized in Table 1. The validity of these parametrizations has been explored in many studies using observations of the Earth's climate[20], numerical models of idealized atmospheres[16,21–24] and oceans[7,25]. But it has proved difficult to obtain a conclusive test, owing to the need to explore a very wide range of parameters, in a system with sufficient physical realism. Here we show results of tests using a general circulation model (GCM) of the Earth's atmosphere[26]. The model includes orography and a full set of physical parametrizations, and is forced by fixed sea surface temperatures and perpetual-January radiative forcing. The candidate length and velocity scales were calculated for model climates with different forcings and boundary conditions (see Methods).

Figure 1 is a plot of the various candidate length scales against a measure of the mean fluid parcel displacement, $L_{\text{disp}} = -\overline{v'T}/(k|v'|\overline{T}_y)$. L_β is the best correlated with L_{disp} (correlation 0.79), although some skill is evident for L_{zone} with a correlation of 0.63. Figure 2 is a plot of the candidate velocity scales against the magnitude of eddy velocity measured in the GCM. Clearly our velocity parametrization is the most accurate with a correlation of 0.96. (The values of correlations quoted here are for the log–log correlation, which are more appropriate for the large range of scales involved. The statistical significance of the correlations was estimated as >99.9% with a Student t-test.)

Combining the length scale L_β with our velocity expression leads to a new parametrization for the heat flux $\overline{v'T'} = k\overline{T}_y^{8/5}(eaq/T_0)^{3/5}(2/\beta)^{4/5}$. Figure 3 is a plot of this parametrization against the horizontal eddy heat flux measured in the GCM runs. The correlation between them is 0.97. A physical picture that is consistent with this scaling is of an upscale turbulent energy cascade that is halted at L_β where nonlinear scale interactions are suppressed. Such a cascade has been proposed by Held and Larichev[6], although they suggested that the throughput of kinetic energy was constrained by baroclinic production, rather than by the heat engine efficiency. Preliminary results[27] suggest that the transport coefficient implied by the above expression for horizontal heat flux may also serve as the basis for expressions for vertical heat flux and for transport of moisture.

As noted earlier, an important prerequisite for the application of a flux-gradient parametrization is that the baroclinic zone be wider than the displacement length[9], L_{disp}. Because the baroclinic zone width in the present climate is about four times L_β, it is reasonable to expect a flux-gradient relationship to hold when averaged over this zone (Fig. 3). Calculations with averaging over latitude bands comparable in size to L_β show similar collapse of the data to that seen in Fig. 3, but there is a suggestion of a systematic variation of slope with latitude, whose significance remains unclear.

A parametrization for eddy heat flux is useful not only for the insight it provides into the workings of the atmosphere, but also for practical climate modelling at a level intermediate between simple energy-balance models and complex GCMs. The heat engine description proposed here gives a thermodynamic constraint on the eddies that allows prediction of the heat transport and pole to Equator temperature difference as well as an estimate of the intensity of mid-latitude storms. Such predictions are not possible with energy-balance models that do not attempt to describe eddy motions at all, and are very expensive with GCMs that explicitly describe every individual eddy. □

Methods

Numerical experiments were performed on the Reading intermediate GCM[26] run at T42 spectral horizontal resolution with 33 vertical levels. This resolution is considered sufficient to represent the global transports by eddies[28]. Each experiment was for 120 d with diagnostics taken from the last 90 d. The experiments were as follows. Radiation experiments: radiative heating rates multiplied everywhere by a constant factor of 0.01, 0.1, 0.5, 1, 2, 3, 5, 10 or 20. Planetary radius experiments: radius increased by a factor of 1.2, 1.4, 1.5, 1.6 or 1.7. Rotation rate experiments: planetary rotation rate increased by a factor of 1.4, 1.6 or 1.7. Temperature gradient experiments: surface temperature gradient multiplied by 0.3, 0.6, 1.2, 1.4, 1.8 or 2. Temperature experiments: surface temperature

changed uniformly by +5 K, −10 K or −20 K. Additional experiments, not presented here, demonstrated insensitivity of the simulated heat fluxes to changes in surface fluxes of heat, moisture and momentum, or in scale-selective dissipation.

Except as noted below, all quantities used to create Figs 1–3 are zonal means, averaged over the mid-latitude region defined as 1,000–200 mbar, 28°–68° latitude, for each hemisphere. The results were found to be insensitive to variations in the definition of the mid-latitude region. In particular, this height is sufficient to include essentially the whole troposphere and all the eddy activity. It should be noted that the average meridional temperature gradient is closely constrained by the fixed surface temperatures, and could be replaced by the surface temperature gradient in the calculations with only a modest loss in accuracy. The diabatic forcing term q includes both the radiative heating averaged over the mid-latitude region and the surface fluxes of sensible heat, although the contribution of surface fluxes turns out to be small. The height scales H and H_s, used to calculate the radius of deformation L_D, and the Charney length scale L_γ, were taken to be constant at 8 km as they did not vary substantially in any of the experiments. In calculating L_γ, the vertical averages were weighted[13] by a factor $e^{-z/D}$, where $D = H_s/(0.48 + 1.48\gamma)$. The latitude of the zonal wind maximum, which did not vary substantially between experiments, was used to calculate f and β. The size of the baroclinic zone, L_{zone}, was defined as the distance between the two latitudes where the strength of the vertically averaged zonal-mean zonal wind first drops to half of its maximum value. In all calculations the correlation coefficient k was given a constant value of 0.25, while the utilization coefficient e was given a constant value of 0.75.

Received 1 November; accepted 18 December 2001.

1. Pierrehumbert, R. T. & Swanson, K. L. Baroclinic instability. *Annu. Rev. Fluid Mech.* **27,** 419–467 (1995).
2. Held, I. M. The macroturbulence of the troposphere. *Tellus A* **51,** 59–70 (1999).
3. Green, J. S. Transfer properties of the large scale eddies and the general circulation of the atmosphere. *Q. J. R. Meteorol. Soc.* **96,** 157–185 (1970).
4. Stone, P. H. A simplified radiative-dynamical model for the static stability of rotating atmospheres. *J. Atmos. Sci.* **29,** 405–418 (1972).
5. Branscome, L. E. A parameterization of transient eddy heat flux on a beta plane. *J. Atmos. Sci.* **41,** 2508–2521 (1983).
6. Held, I. M. & Larichev, V. D. A scaling theory for horizontally homogeneous, baroclinically unstable flow on a beta plane. *J. Atmos. Sci.* **53,** 946–952 (1996).
7. Haine, T. W. N. & Marshall, J. Gravitational, symmetric and baroclinic instability of the ocean mixed layer. *J. Phys. Oceanogr.* **28,** 634–658 (1998).
8. Barry, L., Thuburn, J. & Craig, G. C. GCM tests of some possible dynamical constraints on the mid-latitude atmosphere: The v'–T' correlation, PV homogenisation and the dividing isentrope. *Q. J. R. Meteorol. Soc.* (submitted).
9. Pavan, V. & Held, I. M. The diffusive approximation for eddy fluxes in baroclinically unstable jets. *J. Atmos. Sci.* **53,** 1262–1272 (1996).
10. Eady, E. T. Long waves & cyclone waves. *Tellus* **1,** 33–52 (1949).
11. Charney, J. G. The dynamics of long waves in a baroclinic westerly current. *J. Meteorol.* **4,** 135–162 (1947).
12. Held, I. M. The vertical scale of an unstable baroclinic wave and its importance for eddy heat flux parameterisation. *J. Atmos. Sci.* **35,** 572–576 (1978).
13. Stone, P. H. & Yao, M.-S. Development of a 2-dimensional zonally averaged statistical-dynamic model. 3. The parameterisation of eddy fluxes of heat and moisture. *J. Clim.* **3,** 726–740 (1990).
14. Charney, J. G. Geostrophic turbulence. *J. Atmos. Sci.* **28,** 1087–1095 (1971).
15. Salmon, R. *Lectures on Geophysical Fluid Dynamics* (Oxford Univ. Press, Oxford, 1998).
16. Larichev, V. D. & Held, I. M. Eddy amplitudes and fluxes in a homogeneous model of fully developed baroclinic instability. *J. Phys. Oceanogr.* **25,** 2285–2297 (1995).
17. Rhines, P. B. Waves and turbulence on a beta-plane. *J. Fluid. Mech.* **69,** 417–443 (1975).
18. James, I. N. *Introduction to Circulating Atmospheres* (Cambridge Univ. Press, Cambridge, 1994).
19. Golitsyn, G. S. A similarity approach to the general circulation of planetary atmospheres. *Icarus* **13,** 1–24 (1970).
20. Stone, P. H. & Miller, D. A. Empirical relations between seasonal changes in meridional temperature gradients and meridional fluxes of heat. *J. Atmos. Sci.* **37,** 1708–1721 (1980).
21. Vallis, G. K. Numerical studies of eddy transport properties in eddy-resolving and parameterised models. *Q. J. R. Meteorol. Soc.* **114,** 183–204 (1988).
22. Stone, P. H. & Branscome, L. Diabatically forced, nearly inviscid eddy regimes. *J. Atmos. Sci.* **49,** 355–367 (1992).
23. Panetta, R. L. Zonal jets in wide baroclinically unstable regions: persistence and scale selection. *J. Atmos. Sci.* **29,** 2073–2106 (1993).
24. James, I. N. Two parameterisations of the temperature flux due to baroclinic waves. *Q. J. R. Meteorol. Soc.* **123,** 1–16 (1997).
25. Visbeck, M., Marshall, J. & Haine, T. Specification of eddy transfer coefficients in coarse resolution ocean circulation models. *J. Phys. Oceanogr.* **27,** 381–402 (1997).
26. Forster, P. M. de F., Blackburn, M., Glover, R. & Shine, K. P. An examination of climate sensitivity for idealised climate change experiments in an intermediate general circulation model. *Clim. Dyn.* **16,** 833–849 (2000).
27. Barry, L. *Predicting Eddy Heat Transport in the Troposphere* Thesis, Univ. Reading (2000).
28. Boer, G. & Denis, B. Numerical convergence of the dynamics of a GCM. *Clim. Dyn.* **13,** 359–374 (1997).

Competing interests statement

The authors declare that they have no competing financial interests.

Correspondence and requests for materials should be addressed to G.C.C. (e-mail: G.C.Craig@Reading.ac.uk).

Mid-mantle deformation inferred from seismic anisotropy

James Wookey*, J.-Michael Kendall* & Guilhem Barruol†

* *School of Earth Sciences, University of Leeds, Woodhouse Lane, Leeds LS2 9JT, UK*
† *CNRS, Université Montpellier, 34095 Montpellier, Cedex 05, France*

With time, convective processes in the Earth's mantle will tend to align crystals, grains and inclusions. This mantle fabric is detectable seismologically, as it produces an anisotropy in material properties—in particular, a directional dependence in seismic-wave velocity. This alignment is enhanced at the boundaries of the mantle where there are rapid changes in the direction and magnitude of mantle flow[1], and therefore most observations of anisotropy are confined to the uppermost mantle or lithosphere[2,3] and the lowermost-mantle analogue of the lithosphere, the D″ region[4]. Here we present evidence from shear-wave splitting measurements for mid-mantle anisotropy in the vicinity of the 660-km discontinuity, the boundary between the upper and lower mantle. Deep-focus earthquakes in the Tonga–Kermadec and New Hebrides subduction zones recorded at Australian seismograph stations record some of the largest values of shear-wave splitting hitherto reported. The results suggest that, at least locally, there may exist a mid-mantle boundary layer, which could indicate the impediment of flow between the upper and lower mantle in this region.

Seismic anisotropy in the upper 200 km of the Earth's mantle is primarily attributed to the preferred alignment of olivine crystals which have deformed by dislocation creep[5]. The origin of anisotropy at greater depths is more speculative, but there is evidence for anisotropy in the transition zone in some regions[6–8], but not in others[9,10]. In an effort to reconcile discrepancies in global velocity models derived from body-wave travel times and normal-mode observations, Montagner and Kennett[11] allowed both anisotropy and attenuation in a joint inversion of these data sets. Their final model shows significant levels of anisotropy in the uppermost and lowermost mantle, but also in the vicinity of the 660-km discontinuity (hereafter referred to as the '660'). This motivated an investigation of mid-mantle anisotropy on a regional scale. Here we investigate shear-wave splitting in deep-focus events that image a region below the Australian plate (Fig. 1).

Stations in Australia are ideal for investigating near-source anisotropy, as studies have shown that they exhibit very little, if any, receiver-side shear-wave splitting[12–14] (see Supplementary Information for a summary of observations). For example, 52 SKS measurements with good azimuthal coverage at the station CAN (see Fig. 1 for location) show that shear waves that are travelling nearly vertically are not split while crossing the Australian lithosphere beneath this station[12]. In contrast, we find that deep-focus events from the Tonga–Kermadec and New Hebrides subduction zones show very large degrees of shear-wave splitting at this and four other Australian stations (Fig. 2), suggesting anisotropy deeper in the mantle, away from the receiver.

We made splitting measurements from 92 events, at epicentral distances of 24° to 59° from the Australian stations, using the method of ref. 15, which estimates the time separation between the fast and slow shear wave, δt, and the polarization of the fast shear wave at the receiver, ϕ. This method attempts to remove the anisotropy-induced splitting by minimizing the shear-wave signal in the direction perpendicular to the polarization direction of the shear wave before entering the anisotropic region[16]. A grid search over δt and ϕ is used to estimate the splitting parameters, and a statistical F-test is used to assess errors. The correction for splitting